Naval Information Warfare Center PACIFIC

TECHNICAL REPORT 3268

MARCH 2022

Diagnostic Development for Study of In-Air Laser Induced Plasma

Michael P. Ross, Ph.D
Melvin Pascoguin
NIWC Pacific

Naval Information Warfare Center Pacific (NIWC Pacific)
San Diego, CA 92152-5001

This page is intentionally blank.

TECHNICAL REPORT 3268
MARCH 2022

Diagnostic Development for Study of In-Air Laser Induced Plasma

Michael P. Ross, Ph.D.
Melvin Pascoguin

NIWC Pacific

Administrative Notes:

This report was approved through the Release of Scientific and Technical Information (RSTI) process in October 2021 and formally published in the Defense Technical Information Center (DTIC) in March 2022.

NIWC Pacific
San Diego, CA 92152-5001

NIWC Pacific
San Diego, California 92152-5001

A. D. Gainer, CAPT, USN
Commanding Officer

W. R. Bonwit
Executive Director

ADMINISTRATIVE INFORMATION

The work described in this report was performed by the Atmospheric Propagation Branch of the Communications and Networks Department, Naval Information Warfare Center Pacific (NIWC Pacific), San Diego, CA. Funding for this Basic Research project was provided by the In-House Laboratory Independent Research (ILIR) program sponsored by the Office of Naval Research.

Released by
Phillip Juarez, Division Head
Communications Division

Under authority of
Suzie Hartzog, Department Head
Communications and Networks Department

ACKNOWLEDGMENTS

Special acknowledgment to Dr. Brittany Lynn and Melvin Pascoquin for their assistance in performing the technical work and for working with the Technical Publishing editing team to publish this report to DTIC on behalf of Dr. Michael P. Ross wrote who has moved on in his career and is no longer working at the center.

Editor: RJP

EXECUTIVE SUMMARY

OBJECTIVE

This study aims to explore the feasibility of generating Radio Frequency (RF) signals with laser induced plasma (LIP) in air at atmospheric pressure. This report presents the development status of a suite of diagnostics meant to look for correlations between LIP properties and RF emission. The study aims to control the time dynamics and geometry of LIP to determine if those factors ultimately control RF output. Adjusting the time delay between an ultra-short-pulse-laser (USPL) (35 fs pulse duration and 6 mJ pulse energy) and a Nd:YAG laser (ns pulse duration and up to 700 mJ pulse energy) allows control over the time dynamics. A spatial light modulator (SLM) provides control of the plasma geometry.

RESULTS

- An experimental test bed has been constructed consisting of synchronized USLP and Nd:YAG lasers, optics aligned for combining the laser pulses, plasma diagnostics, and motorized translation stages for holding solid targets.
- A laser interferometer has been constructed capable of measuring electron density in LIP with spatial resolution near 10 μm and time resolution near 10 ps.
- An astigmatism-corrected 320 mm focal length spectrometer has been acquired and integrated with an ICCD, input fiber bundle, and collection optics to serve as a passive spectroscopy diagnostic with 200 μm spatial resolution. This instrument can deliver electron density and electron temperature measurements if appropriate plasma modeling is applied to interpret the spectra.

RECOMMENDATIONS

Upcoming experiments will measure the scaling of RF enhancement as a function of the laser intensities as well as their relative time delay. Plasma diagnostics will look for correlation between RF enhancement and plasma properties.

Diagnostic development is ongoing, and refinement will continue. Determining accurate measures of electron density and electron temperature from spectral observations will require deeper examination of the plasma modeling employed to interpret the measurements. Further exploration of interferometric methods to enable transverse-viewing could be worthwhile in order to reduce measurement ambiguity. Acquiring an additional amplifier for the USPL would help the research effort because generating LIP in air alone using focal lengths greater than 500 mm is difficult with the present laser intensity.

This page is intentionally blank.

CONTENTS

Figures

This page is intentionally blank.

1. INTRODUCTION

1.1 PURPOSE OF THIS DOCUMENT

This report documents the experimental test bed including triggering mechanisms and instrumentation constructed to study RF emission by laser induced plasma (LIP). One aim of the document is to include enough detail and background information to assist future researchers replicating the diagnostic tools.

1.2 DOCUMENT STRUCTURE

The document begins by exhibiting potential applications of laser induced plasma RF emission and by elucidating subtle distinctions between LIP generation mechanisms based on laser and target type. Then, the report documents practical findings related to the test bed construction and to the operation of the plasma diagnostics.

1.3 SUMMARY OF FINDINGS

A new test bed has been constructed at NIWC Pacific for the study of RF emission by LIP. A laser interferometer capable of measuring time-and-space-resolved electron densities has been built, and a passive optical emission spectroscopy system has been implemented. Future work will employ these diagnostics to relate RF emission to measured plasma properties.

This page is intentionally blank.

2. BACKGROUND

LIPs in air can generate RF radiation with characteristics that may be influenced by the plasma properties, which in turn can be controlled by adjusting characteristics of the laser pulse. Some LIPs generate broadband RF emission, [1, 2] so they could in principle provide adjustable RF sources for directed emission at selected frequencies. Arrays of log-periodic dipole antennas have been applied to steer RF emission in the 6–16 GHz band [3], and study of such arrays remains an active area of research [4, 5]. The feasibility of RF beamforming with LIPs is bolstered by positive results from studies examining acoustic beamforming with LIPs. Because LIPs can act as acoustic point sources [6], arranging multiple, discrete LIPs in a volumetric array can provide a directional and steerable sound source. The feasibility of such beamforming has been verified by sequentially generating each plasma in such an array one at a time and then combining acoustic measurements of each plasma to test a beamforming algorithm to locate reflections [7]. Figure 1 illustrates a basic cartoon illustration of a potential RF beamforming concept with LIP. Assuming the LIP act as isotropic point sources and considering only one RF frequency, the effective transmit antenna pattern at that frequency of two adjacent LIP generated at the same instant will look like that shown in the left image. If the LIP are instead generated at disparate times separated by 90-degrees in phase with respect to the RF frequency of interest, the effective antenna pattern will turn to act as the one in the image at right. By continuously tuning the delay time between the generation of the two plasmas, the direction of the effective antenna pattern can in principle be directed through a continuous range of orientations.

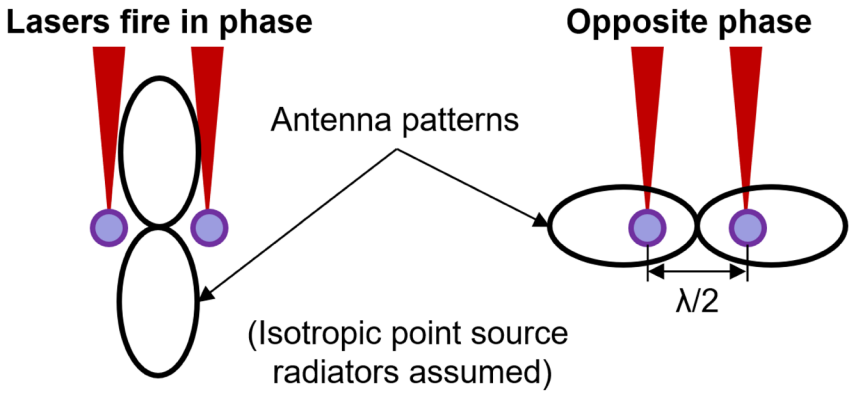

- Left: The effective antenna pattern resulting from two adjacent LIPs generated at the same instant, each modeled as isotropic point source radiators of a single RF frequency. The wavelength, λ, of that RF frequency is taken to define the spacing between the adjacent LIP.
- Right: The effective antenna pattern from two adjacent LIPs generated at different times separated by 90-degrees of phase with respect to the RF frequency of interest.

Figure 1. LIPs could prove potentially useful in RF beam forming.

A major application of LIPs is laser induced breakdown spectroscopy (LIBS) for (relatively) non-destructive materials identification [8, 9], which could be helpful in identifying hazardous materials or camouflaged objects at a distance. The RF emission from LIP is in a range useful for ground penetrating radar [10] with obvious utility for mine detection. Many other diverse applications of LIPs exist including X-ray production for laboratory instrumentation [11] and terahertz radiation production for use in medical and scientific instruments [12] .

This study considers LIP generated by a Coherent Astrella USPL (35 fs, 6 mJ maximum pulse energy) and a Continuum Surelite EX Nd:YAG laser (1 ns, 700 mJ maximum pulse energy). This effort generates

LIP in air alone as well as in air on solid targets as illustrated in Figure 2. The disparate natures of the timescales of the USPL and Nd:YAG laser pulses as well as differences between types of targets cause a variety of plasma formation mechanisms as well as a range of plasma properties. USPL have sufficient photon fluence to ionize air through multi-photon ionization and tunnel ionization, while ns laser pulses need some initial source of electrons (i.e.: from dust particles or a solid target surface) to initiate avalanche ionization. Considering solid targets, the time duration of the pulses affects the ablation and ionization processes. For instance, on a solid insulating target, a USPL pulse ejects electrons from the target surface via multi-photon ionization so quickly that the resulting electric field induced by charge separation between those electrons and ions remaining in the solid material pulls the ions out of the target. On metal insulating targets, the target material is energized faster than the surface can evaporate, which builds up pressure in the material leading to Coulomb explosion resulting in plasma generation [13]. Conversely, for ns pulse interactions with solid targets, thermal heating plays a larger role in the ionization process. Solid targets absorb ns laser energy via inverse bremsstrahlung (IB), which initially heats only the electrons. Sufficient time passes during a ns pulse for the electrons to transfer their energy to the surrounding material lattice and ultimately heat the material leading to ionization [14].

USPLs deliver sufficient power to induce non-linear optical effects resulting in filamentation [15] whereby the interplay of the non-linear Kerr effect and refraction due to the presence of plasma electron density allows high laser intensities to extend over ranges far exceeding the Rayleigh range of the focusing system. Observing this process orthogonally to the propagation direction of the laser using a camera with an exposure time longer than the duration of these dynamics records an extended conical emission of visible light called a filament. Plasma filaments exhibit electron densities of $1 \times 10^{14} - 1 \times 10^{18}$ cm^{-3} and initial electron temperatures on the order of a few eV [15]. Electron density rises during ionization, which occurs during the laser pulse duration, and it decays on the order of the electron recombination time in air, dropping by an order of magnitude in around 1 ns [16]. The temperature decays during a longer time period taking 10 ns to drop by an order of magnitude [17]. Properties of LIP generated by ns lasers differ somewhat from those generated by USPL. LIP generated on a Pd metal target by a 100 mJ, 10 ns Nd:YAG pulse reaches electron temperatures around 0.4-0.6 eV and electron densities of $6{\times}10^{17}$ cm^{-3}, which persist over the course of μs timescales [18]. In the case of a ns pulse, observed electron densities and temperatures generated on metal targets are twice the values observed in air alone, where ionization is presumably seeded by dust particulates.

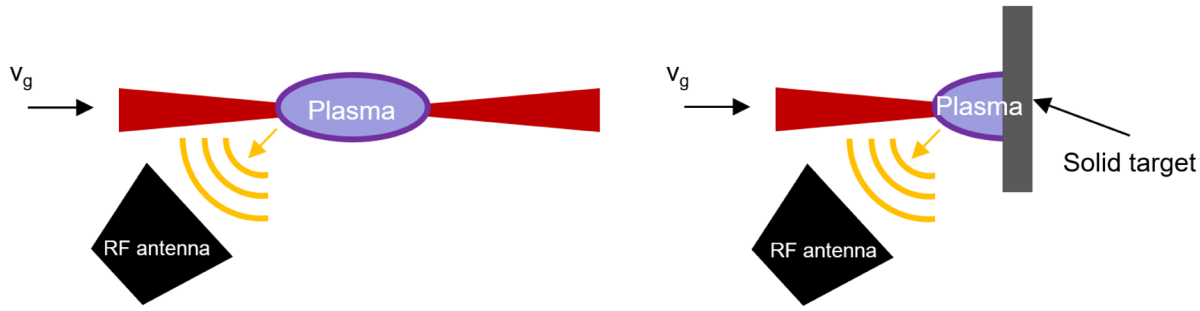

- Left: Plasma generated in air alone by focused laser pulse propagating from left to right.
- Right: Plasma generated in air on a solid target by focused laser. Solid target materials under study include electrically-conductive metals like aluminum, titanium, stainless steel, and copper as well as electrically-insulating materials like nylon and Teflon.

Figure 2. Illustrations of the main laser induced plasma geometries studied in this report in which an RF antenna measures emission.

Employing ns and fs laser pulses together in tandem provides a way to affect the plasma dynamics and resulting RF emission. Overlapping focused fs and ns pulses on a metal target enhances enhances the RF emitted signal by an order of magnitude when forming plasma on metal target surfaces [19]. The fs pulses form an initial seed plasma, which is then heated by the ns plasma. The specific mechanisms involved in this enhancement are still an unresolved matter, which the present effort aims to explore.

This page is intentionally blank.

3. EXPERIMENTAL METHODS

3.1 TEST SETUP

An experimental test bed has been constructed to facilitate experimental observations of RF emission by LIP. The optical arrangement combines USPL and Nd:YAG pulses by using a dichroic mirror as shown in Figure 3. The USPL is expanded to allow use of a spatial light modulator (SLM) to control the focal geometry of the USPL laser pulse. The SLM adjusts the wavefront of the USPL pulse by applying phase shifts that spatially vary across the laser beam cross-section [20]. The SLM's damage threshold requires the USPL beam be expanded to 18 mm diameter to minimize incident intensity. Ten percent of the USPL pulse is split from the plasma-generating pump beam to act as an interferometry beam. Spectroscopy collection optics and an RF directional antenna are mounted near the plasma formation region to make observations. Blocking RF noise pickup from the Nd:YAG laser's Q-switch by the RF antenna required placement of RF electromagnetic impulse (EMI) absorbing foam on the surface of the test bed's optics table in the vicinity of the RF antenna and plasma.

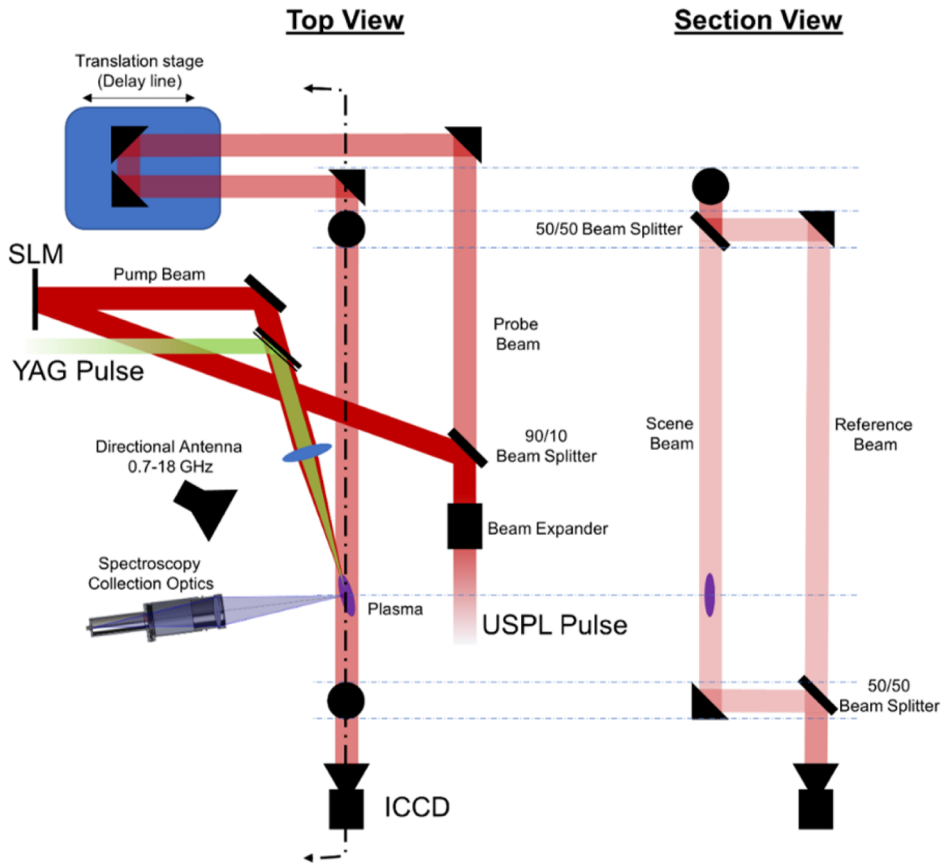

- Left: A top view illustrating how a dichroic mirror allows the combination of the USPL and Nd:YAG pulses. A beamsplitter diverts 10 percent of the USPL as a probe beam for use in a Mach-Zehnder style interferometer. A translation stage functions in a delay line that can span up to a 1 ns time delay between plasma initiation and interferometry measurement. A spatial light modulator (SLM) is included in the setup to allow control of the USPL wavefront and thereby the plasma geometry.
- Right: A view of the section indicated by the bracket with arrows in the top view highlights the Mach-Zehnder geometry of the interferometer.

Figure 3. Experimental set up employed in this study.

Synchronizing the USPL and Nd:YAG lasers in time required detailed understanding of the triggering mechanisms in each system, and this report recounts various attempts to synchronize the lasers to inform future users of these systems. Initially, a central Stanford Research Systems DG 535 delay generator supplied trigger pulses to both lasers, but the resulting jitter in the actual USPL trigger time exceeded 10 ns, which is too high for this study as RF enhancement during dual pulse operation is sensitive to time delay changes on the order of 1 ns. This jitter occurred because the USPL is pumped by a diode laser with an 80 MHz repetition rate. Any external trigger causes the USPL to deliver the next pulse in that 80 MHz pulse train, and the period of that 80 MHz pulse train is 12.5 ns, which explains the jitter observed. The next attempted triggering arrangement attempted to use the USPL to trigger the delay generator, which would in turn trigger the Nd:YAG. The Nd:YAG requires two trigger inputs: one triggers the flashlamp, and the other triggers the Q-switch. The flashlamp trigger must precede the Q-switch by 175 μs. The USPL can deliver various sync output signals, but they can only be tuned to leave the laser on the order of 14 μs in advance of the corresponding light pulse. The first attempts at using this arrangement to synchronize a given USPL pulse, used the sync output from the preceding USPL pulse to trigger both the flashlamp and Q-switch in the Nd:YAG. Doing this indeed provided control over the relative delay between the Nd:YAG and USPL, but a significant drift in that time delay appeared on the order of 1 ns of drift for every minute of observation. That amount of drift make experiments intractable. The final triggering arrangement, which provided control of the time delay without drift with jitter of $\pm$ 1.5 ns, triggered the Nd:YAG flashlamp using the sync out of the preceding USPL pulse while triggering the Nd:YAG Q-switch with the sync out of the USPL pulse we desire to synchronize. Figure 5 shows photodiode signals from the USPL and YAG averaged over 50 pulses and shows distributions of the signal peaks to illustrate the jitter involved. This final triggering method does introduce drift between the Nd:YAG flashlamp and Q-switch, but that drift is insignificant compared to the timescale of the population inversion build up from the flashlamp firing. Ultimately, the Q-switch attempts to time laser firing at the peak in the population inversion, and the timing requirements to match the peak are on the order of μs.

One of the biggest challenges to overcome at this juncture is the non-repeatable location of plasma formation when running the Nd:YAG laser. While running with or without solid targets, the location and geometry of the plasma generated by the Nd:YAG varies up to multiple cm along the laser propagation direction, and the generated plasma can be composed of multiple bright spots. This has major ramifications for the effectiveness of interferometry and spectroscopy as knowing the plasma geometry is necessary to convert line-integrated measurements to electron density and temperature profiles, and collecting sufficient spectroscopy signals depends on forming a plasma consistently where spectroscopy collection optics are aimed. The repeatability may be improved by expanding the Nd:YAG beam prior to its passage through the final focusing lens to effectively decrease the focusing f-number. Relatively high f-number focusing may simply leave too much laser intensity distributed over too long of a cylindrical volume in the plasma formation region to encourage repeatable generation. Another major challenge is apparently weak (in terms of both light emission and plasma density) plasma formation by the USPL pump beam alone. This issue has been partially assuaged by temporarily replacing the SLM in the experimental set up with a flat, 0-degree angle of incidence mirror. The SLM caused enough diffractive scattering to reduce the laser pulse energy by more than a factor of 2. Using the flat mirror saves that loss, but we still experience significant loss at the dichroic mirror that merges the Nd:YAG pulse with the USPL. That dichroic mirror is 1-inch diameter and must be oriented at a 45-degree angle relative to the USPL pulse. Therefore, it clips significant portions of the USPL pump pulse. A custom 2-inch diameter dichoric mirror has been purchased, which should eliminate all clipping loss of the USPL pump pulse. Nonetheless, future experiments could be bolstered by the addition of an additional amplifier for the USPL laser.

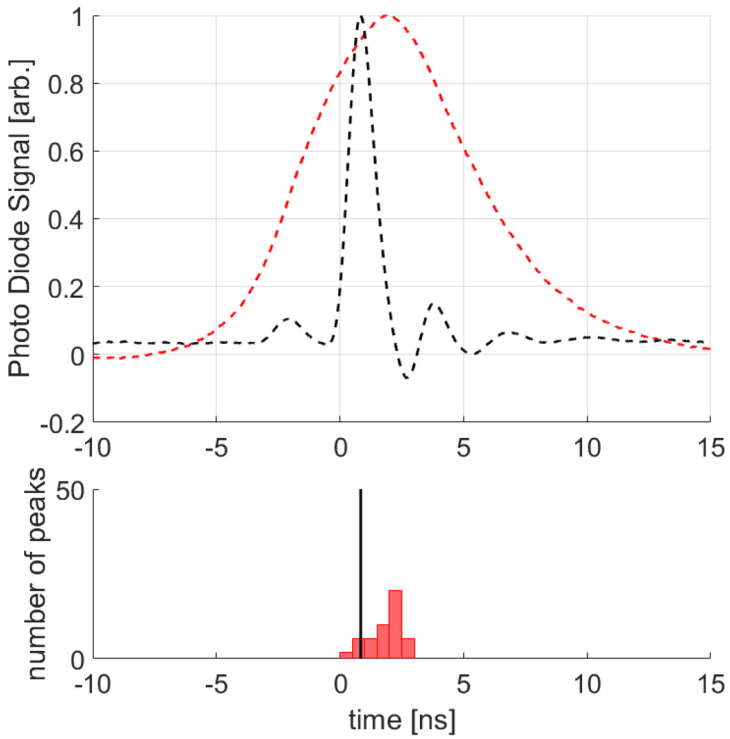

- Top: Photo diode signals from the USPL (black) and YAG (red) averaged over 50 laser pulses.
- Bottom: Histograms showing where the peaks in the photo diode signals resided in time for the 50 laser pulses. In this case, the digitizing scope was triggered off the USPL photodoiode, so all its peak fall into one narrow bin. The peak in the YAG photodiode signal exhibited some drift on the order of $\pm$ 1.5 ns.

Figure 4. Measurements characterizing the synchronization of USPL and Nd:YAG lasers.

3.2 LASER INTERFEROMETRY

The Mach-Zehnder interferometer pictured in the section view of Figure 3 allows measurement of electron density with 10 μm and 10 ps resolution. The instrument directly measures the phase shift imparted on a laser beam line-integrated along the laser's path through the plasma. The phase shift imparted to a laser pulse of wavelength λ by a plasma with electron density n_e is

$$\phi_{n_e} = -\frac{e^2}{4\pi c^2 m_e \epsilon_o}\lambda \int n_e dl \tag{1}$$

where e is the electron charge, c is the speed of light, m_e is the electron mass, ϵ_0 is the permittivity of free space, and the integration is performed over the laser's path. The sensitivity of an interferometer to a given n_e depends on the path length, which ultimately derives from the optical set up. Figure 6 illustrates the phase shift as a function of n_e and integrated path length assuming a spatially-uniform plasma density. With the optical set up employed here, phase shifts down to 0.05-0.1 are detectable. Based on optical imaging, the USPL plasma filaments generated here are likely near 100 μm in diameter, which means filament electron densities would have to be around $10^{18} - 10^{19}$ [cm^{-3}] to be detected with interferometer beams transverse to the plasma's longitudinal axis. Such densities are on the high end of those detected in plasma filaments and are usually only detected for short pump beam focal lengths (50 mm)[21]. Using an oblique geometry like that shown in Figure 3 where the probe beam approaches the plasma formation

region at a 3-degree angle with respect to the USPL pump beam increases the sensitivity of the diagnostic to electron density by approximately a factor of 20 over that of a transverse beam arrangement by increasing the integrated path length. Other authors indicate measurements of n_e down to 2-3 $\times 10^{16}$ cm $^{-3}$ in plasma filaments of 150 μm diameter with transverse beam paths, which implies phase shift sensitivity below 0.05, but those authors employ a telescope to magnify the interferograms 8 times, which may explain the improved sensitivity [16]. A form of in-line holography can reportedly measure electron densities below 10^{16} cm^{-3} even with a transverse line of view. This technique only uses a scene beam and therefore alleviates the difficulty of aligning a Mach-Zehnder interferometer with a laser of coherence length less than 10 μm [22]. However, extraction of the measured phase shifts requires different analysis routines than are easily available.

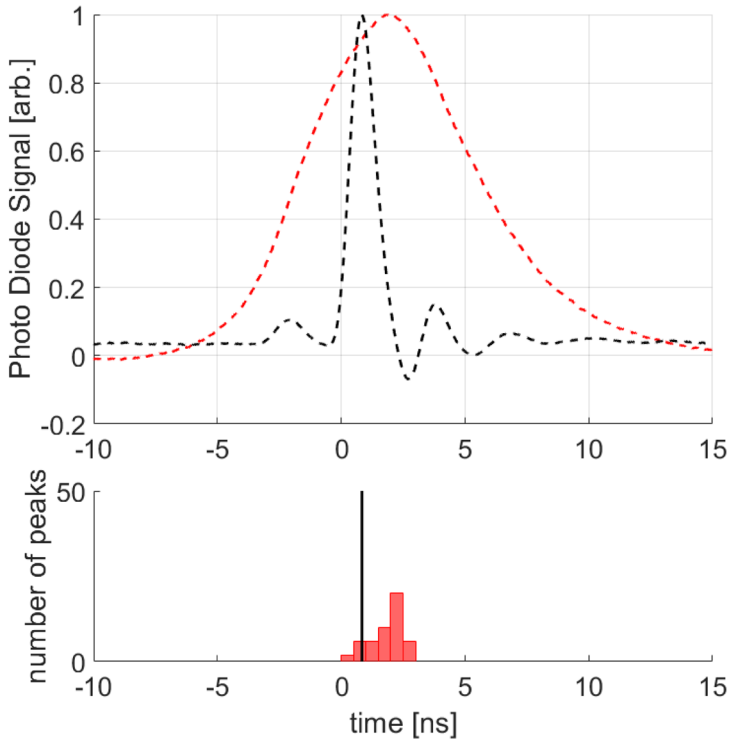

- Top: Photo diode signals from the USPL (black) and YAG (red) averaged over 50 laser pulses.
- Bottom: Histograms showing where the peaks in the photo diode signals resided in time for the 50 laser pulses. In this case, the digitizing scope was triggered off the USPL photodoiode, so all its peak fall into one narrow bin. The peak in the YAG photodiode signal exhibited some drift on the order of $\pm$ 1.5 ns.

Figure 5. Measurements characterizing the synchronization of USPL and Nd:YAG lasers.

One of the biggest challenges to overcome at this juncture is the non-repeatable location of plasma formation when running the Nd:YAG laser. While running with or without solid targets, the location and geometry of the plasma generated by the Nd:YAG varies up to multiple cm along the laser propagation direction, and the generated plasma can be composed of multiple bright spots. This has major ramifications for the effectiveness of interferometry and spectroscopy as knowing the plasma geometry is necessary to convert line-integrated measurements to electron density and temperature profiles, and collecting sufficient spectroscopy signals depends on forming a plasma consistently where spectroscopy collection optics are aimed. The repeatability may be improved by expanding the Nd:YAG beam prior to its passage through the

final focusing lens to effectively decrease the focusing f-number. Relatively high f-number focusing may simply leave too much laser intensity distributed over too long of a cylindrical volume in the plasma formation region to encourage repeatable generation. Another major challenge is apparently weak (in terms of both light emission and plasma density) plasma formation by the USPL pump beam alone. This issue has been partially assuaged by temporarily replacing the SLM in the experimental set up with a flat, 0-degree angle of incidence mirror. The SLM caused enough diffractive scattering to reduce the laser pulse energy by more than a factor of 2. Using the flat mirror saves that loss, but we still experience significant loss at the dichroic mirror that merges the Nd:YAG pulse with the USPL. That dichroic mirror is 1-inch diameter and must be oriented at a 45-degree angle relative to the USPL pulse. Therefore, it clips significant portions of the USPL pump pulse. A custom 2-inch diameter dichoric mirror has been purchased, which should eliminate all clipping loss of the USPL pump pulse. Nonetheless, future experiments could be bolstered by the addition of an additional amplifier for the USPL laser.

3.3 LASER INTERFEROMETRY

The Mach-Zehnder interferometer pictured in the section view of Figure 3 allows measurement of electron density with 10 μm and 10 ps resolution. The instrument directly measures the phase shift imparted on a laser beam line-integrated along the laser's path through the plasma. The phase shift imparted to a laser pulse of wavelength λ by a plasma with electron density n_e is

$$\phi_{n_e} = -\frac{e^2}{4\pi c^2 m_e \epsilon_o}\lambda \int n_e dl \tag{2}$$

where e is the electron charge, c is the speed of light, m_e is the electron mass, ϵ_0 is the permittivity of free space, and the integration is performed over the laser's path. The sensitivity of an interferometer to a given n_e depends on the path length, which ultimately derives from the optical set up. Figure 6 illustrates the phase shift as a function of n_e and integrated path length assuming a spatially-uniform plasma density. With the optical set up employed here, phase shifts down to 0.05-0.1 are detectable. Based on optical imaging, the USPL plasma filaments generated here are likely near 100 μm in diameter, which means filament electron densities would have to be around $10^{18} - 10^{19}$ [cm^{-3}] to be detected with interferometer beams transverse to the plasma's longitudinal axis. Such densities are on the high end of those detected in plasma filaments and are usually only detected for short pump beam focal lengths (50 mm)[21]. Using an oblique geometry like that shown in Figure 3 where the probe beam approaches the plasma formation region at a 3-degree angle with respect to the USPL pump beam increases the sensitivity of the diagnostic to electron density by approximately a factor of 20 over that of a transverse beam arrangement by increasing the integrated path length. Other authors indicate measurements of n_e down to 2-3 $\times 10^{16}$ cm $^{-3}$ in plasma filaments of 150 μm diameter with transverse beam paths, which implies phase shift sensitivity below 0.05, but those authors employ a telescope to magnify the interferograms 8 times, which may explain the improved sensitivity [16]. A form of in-line holography can reportedly measure electron densities below 10^{16} cm^{-3} even with a transverse line of view. This technique only uses a scene beam and therefore alleviates the difficulty of aligning a Mach-Zehnder interferometer with a laser of coherence length less than 10 μm[22]. However, extraction of the measured phase shifts requires different analysis routines than are easily available.

Raw data from the interferometer appears as interferograms like those in Figure 7. The parallel fringes in the interferograms occur due to constructive and destructive interference between the interferometer's scene and reference beams. For the diagnostic to work, the path lengths of the two beams must match within a coherence length. A rough upper bound on the coherence length is the total spatial length of each USPL pulse, which is about 10 μm, and in practice, the beams must be aligned so their path lengths match within a few μm for interferogram formation. Stable optical mounts and one translation stage with fine

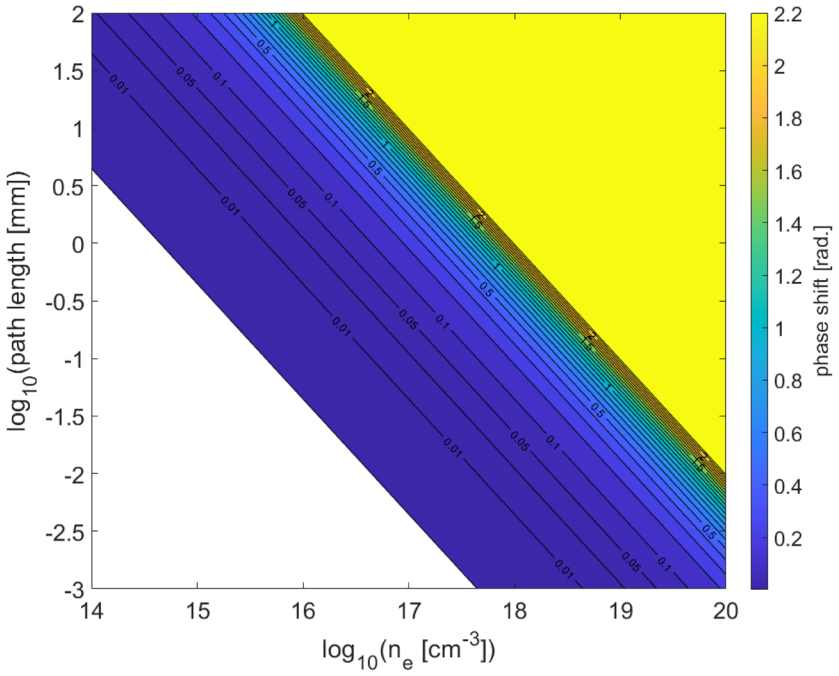

[h]

- Observations of fringe shifts can detect phase shifts down to 0.05-0.1 radians.
- Rearranging the interferometer geometry can extend the interaction path length to increase the instrument's sensitivity to a given n_e.

Figure 6. Phase shift due to electron density n_e imparted on a $\lambda = 800$ nm laser pulse as a function of interaction path length.

adjustment on the reference beam mirror were critical to generating interferograms. Baseline interferograms determine a reference fringe pattern corresponding to zero plasma density, and plasma interferograms ultimately capture the phase shift effect of plasma density as fringe shifts away from the reference fringe pattern. Interferometric Data Evaluation Algorithms (IDEA) software produced and distributed by the Technical University of Graz provides a user-friendly means of analyzing batches of such interferograms to extract 2D maps of phase shift from the fringe modulations. Figure 8 illustrates resulting phase maps. The left image in Figure 8 shows the phase difference between two baseline interferograms, which are taken in the absence of any plasma generation. Interferometers can detect gradients in neutral gas density in addition to electron density. Therefore, to be sure that this interferometer does not mistake air currents or temperature gradients in the ambient laboratory air, the phase shifts between many baselines was compared to characterize its behavior in the absence of plasma generation. The maps of phase difference between baseline interferograms are remarkably uniform across 20 tested baselines with the phase difference map in the left image of Figure 8 being representative of the full data set. In contrast to the spatially uniform phase shifts seen between baselines, the phase difference between plasma interferograms and baselines are significant. The image at right in Figure 8 shows the kind of phase shift caused by the presence of plasma typical in the initial data. To convert these phase differences to volumetric electron density (in units electrons per unit volume) more work is required to estimate the axial extent of the plasma. This will be performed by employing a side-on camera, which will measure the axial extent of

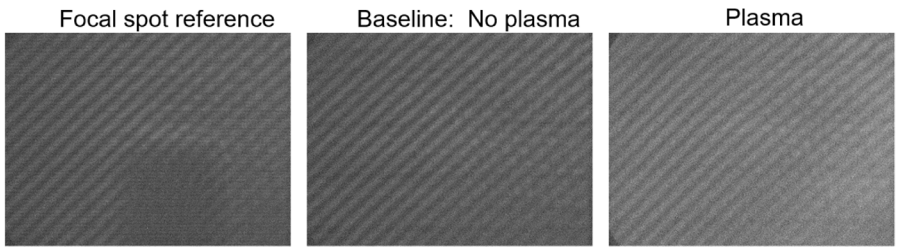

- Left: Baseline interferogram with silhouette of an 8-32 screw positioned at the lens focus where plasma generation nominally occurs to determine image center corresponds with plasma formation region.
- Center: Baseline interferogram without plasma generation gives reference fringe pattern corresponding to zero density.
- Right: Interferogram with plasma present exhibits fringe shifts due to plasma density. This interferogram was acquired during plasma generation with the Nd:YAG alone at a delay time of 0.3 ns, so the USPL probe arrived 0.3 ns after the Nd:YAG pump.

Figure 7. Raw interferograms from the interferometry measurement. Phase shift contained in plasma interferograms can be converted to electron density.

plasma fluorescence. The ability of the diagnostic to discriminate between plasma and no plasma is a vital step in acquiring publishable results and indicates that the diagnostic is operating correctly.

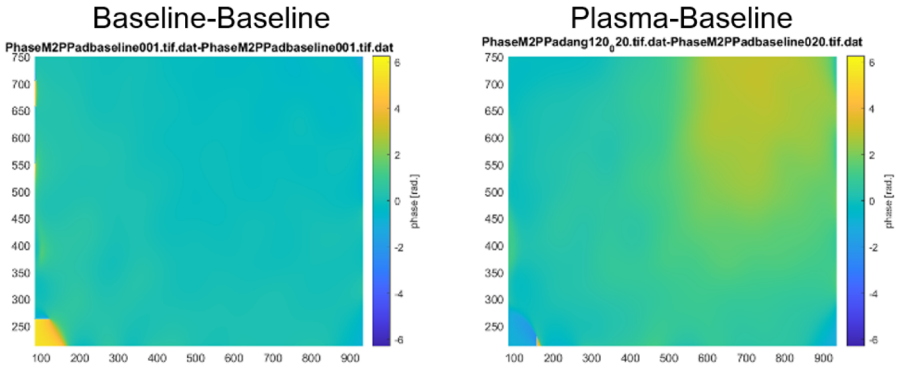

- Left: Phase shift between two baseline interferograms as computed by IDEA software indicates a flat spatial profile expected with a lack of plasma density.
- Right: Phase shift between a plasma interferogram and a baseline interferogram shows spatial variations in phase shift corresponding to plasma density.

Figure 8. Phase shifts computed from raw interferograms from the interferometer.

An adjustable delay line actuated with a translation stage gives the interferometer its time resolution. The translation stage can span a full 30 cm range in sub-mm steps giving it an ability to span 2 ns in time with resolution on the order of about 10 ps. The instrument is set to span from -1.1 to 0.8 ns after the arrival of the USPL pump beam at the pump focus; negative timings could be of interest when studying the interaction of the Nd:YAG pump pulse arriving ahead of the USPL pump pulse. Care was taken to discriminate between observations of electron density and those of neutral gas dynamics. When running the USPL at repetition rates above 100 Hz, the interferometer observes large phase shifts corresponding to hydrodynamic phenomena generated by previous laser pulses. Running the laser below 100 Hz repetition rate allows sufficient time for such hydrodynamic effects to settle prior to the next laser pulse, so running at

low repetition rates is critical for ensuring measurements of phase shift can unambiguously be ascribed to electron density.

3.4 PASSIVE SPECTROSCOPY

Passive optical emission spectroscopy provides electron density and electron temperature, T_e, measurements. As applied here, a lens images light emitted by the LIP onto a bundle of seven 200 μm-diameter fibers, which then convey the light to a Princeton Instruments Isoplane 320 spectrometer shown in Figure 9. The spectrometer uses a diffraction grating to disperse the spectral components of the input light and then directs the light to an ICCD fast framing camera. The ICCD simultaneously records spectra from the seven fibers. Qualities of the spectral output indicate the plasma properties if the plasma conditions fall within certain bounds. Because the light imaged on each fiber comes from a different location in the plasma, this arrangement provides spatial resolution of the measured properties on the order of the fiber diameter. Figure 10 shows a raw image from the ICCD camera showing seven adjacent spectra, each from a different spatial location.

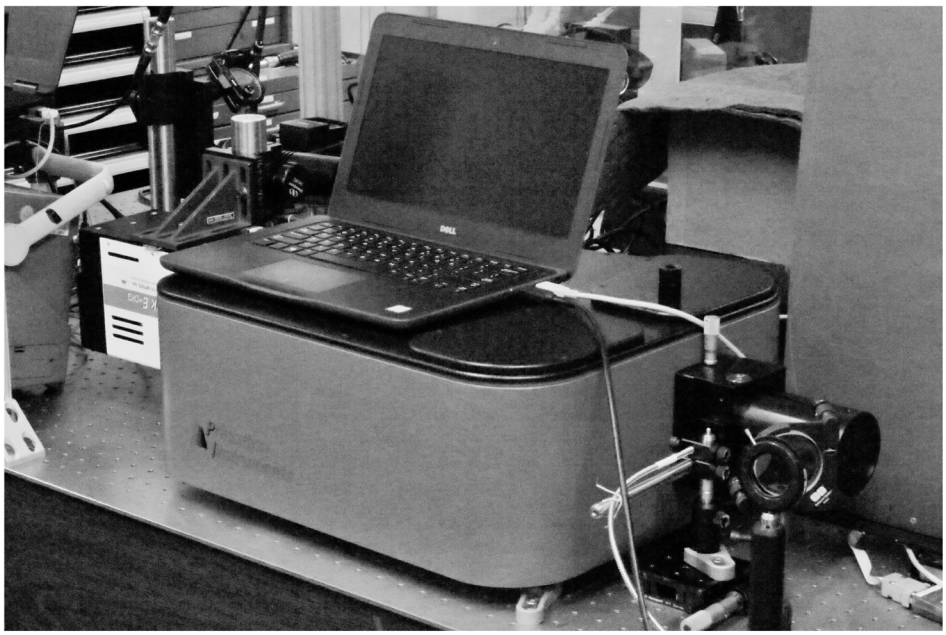

- An ICCD has been integrated with the spectrometer as well as collection optics and a seven-fiber fiber bundle for directing light to the instrument..

Figure 9. Princeton Instruments Isoplane 320 spectrometer acquired this year and employed for passive optical emission spectroscopy measurements.

The analysis methods employed to extract n_e and T_e from measured spectra in LIP similar to those studied here have relied on assuming the plasma behaves as in a local thermodynamic equilibrium (LTE) model [23],[24]. In a plasma in LTE, the populations of atomic energy states for a given ionization state (i.e.: NI, NII, OI, OII, etc.) follow a Boltzmann distribution as in

$$I_{ik} = cA_{ik}g_k \exp\left(-E_k/kT\right) \tag{3}$$

where subscript i indicates the lower energy state, subscript k indicates the upper energy state, A_{ik} is the Einstein coefficient for spontaneous emission of the k-i transition, $g_k = 2J_k + 1$ is the degeneracy factor of

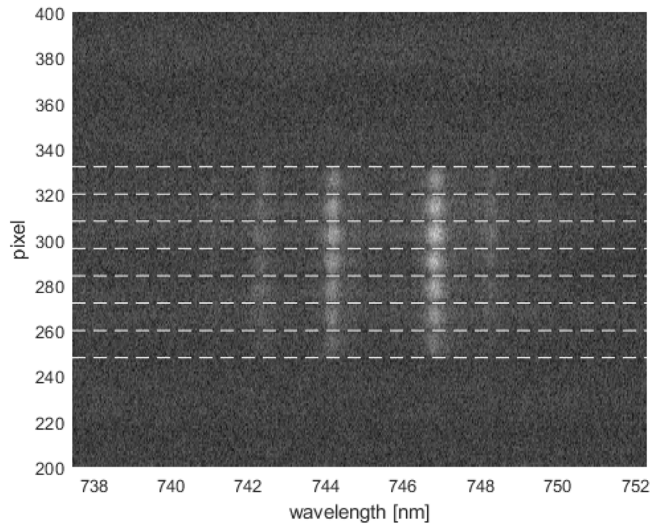

- An ICCD image collects spectra from seven adjacent fibers in a fiber bundle used to direct light from the plasma to the spectrometer. Horizontal white dashed lines demarcate the bounds of each fiber. .
- Each fiber measures light output from a different spatial location.

Figure 10. Raw data from the spectrometer observing a NI triplet at 742.4, 744.2, and 746.8 nm.

the upper state, E_k is the upper state energy, k is Boltzmann's constant, c is a calibration factor, and T is the temperature of that ion species. Taking the natural logarithm of both sides of Equation 3 yields

$$\ln\left(\frac{I_{ik}}{A_{ik}g_k}\right) = -E_k/kT + \ln(c), \tag{4}$$

which indicates the ion temperature can be found as the slope of a plot of $\ln(I_{ik}/A_{ik}g_k)$ versus E_k. Depending on electron-ion and ion-ion collisions rates, the indicated temperature can indicate T_e and/or other ion temperatures in addition to the temperature of the ion species specific to the considered spectral lines.

This Boltzmann plot analysis method only works given LTE conditions. LTE conditions can be evaluated with multiple methods. The McWhirter criterion,

$$n_e \geq 1.6 \times 10^{12} T^{1/2} \Delta E^3, \tag{5}$$

is sufficient but not necessary for LTE to hold. Here, plasma temperature T is in Kelvin, and ΔE^3 is the largest energy transition under consideration in eV. To supplement the McWhirter criterion, other researchers have employed measurements of peak to background (P/B) ratios of spectral lines of interest to provide a stricter indicator on the applicability of LTE. Generally, the P/B ratio starts low, rises to some maximum value, and then decreases. The plasma state is likely to deviate from LTE after the P/B ratio reaches its peak, which provides further evidence for when LTE may be breached [18]. To more definitively determine the plasma temperature, this study will examine applying non-LTE collisional-radiative models describing the populations of atomic energy states. Computational software applications of such models include FLYCHK and PrismSPECT, which can provide line intensity ratios reflective of plasma even in non-LTE conditions.

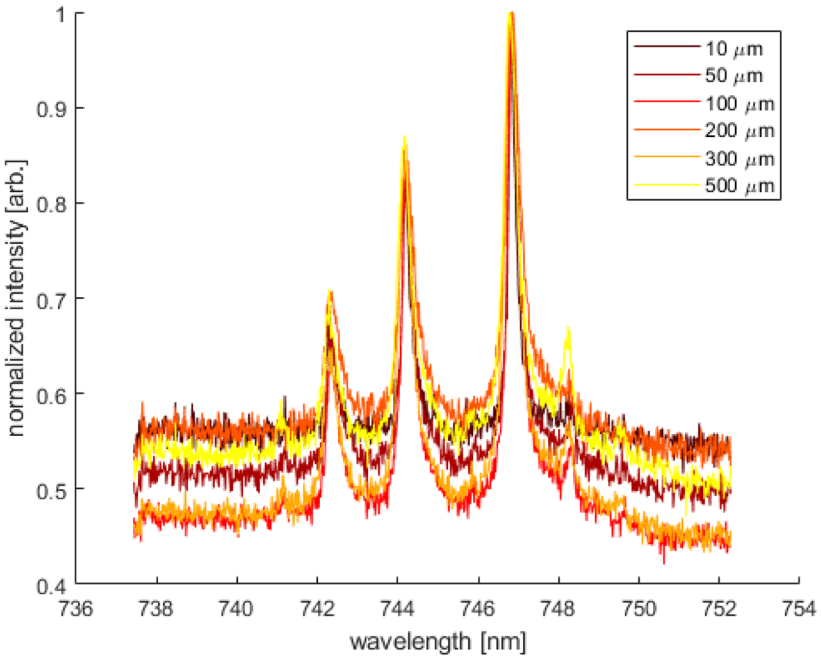

- These spectra have been averaged across the width of that central fiber bin..
- Each spectrum corresponds to a different entrance slit width, which illustrates how the observed spectra are a function of the instrument's properties..

Figure 11. Spectra taken from the central fiber of Figure 10.

The electron density can be estimated from observations of Stark broadening whereby the line width of spectral lines increases due to electric fields from free electrons affecting the energy states of the bound electrons emitting line radiation. Stark broadening dominates other broadening mechanisms such as Doppler broadening due to temperature and in plasma pressure broadening due to collisions with neutrals for this regime of plasma [18]. An OI triplet at 777.4 nm has been used to measure n_e from Stark broadening. The electron density relates to the spectral broadening as in

$$\Delta\lambda_{OI} = 2\omega_{OI} \exp\left(\frac{n_e}{10^{16}}\right), \tag{6}$$

where $\omega_{OI} = 0.0116$ nm is the electron impact parameter [25]. This affect does not require LTE, and it can observe densities down to about 1×10^{16} cm^{-3}.

Successful analysis of Stark-broadened spectra requires the separation of the Stark-broadening from instrument broadening. Figure 11 illustrates instrument broadening by showing how by changing the entrance slit-width, the resulting spectral line widths change. The spectra shown are taken from Figure 10 averaged across the entire bin of the central fiber. The spectral resolution evident in Figure 10 of 0.02 nm is better than that employed by others to detect Stark broadening [25]. De-convolution of Stark and instrument broadening is typically performed by leveraging how Stark broadening exhibits a Lorentzian profile shape while instrument broadening shows a Gaussian shape. This can be performed with methods utilizing Voight profiles, which are a convolution of Lorentzian and Gaussian profiles [26].

Prior to obtaining the Isoplane spectrometer at the end of this year, this effort proto-typed spectroscopy by coupling an ICCD with a DigiKrom-240 Czerny-Turner monochromator (0.06 nm spectral resolution

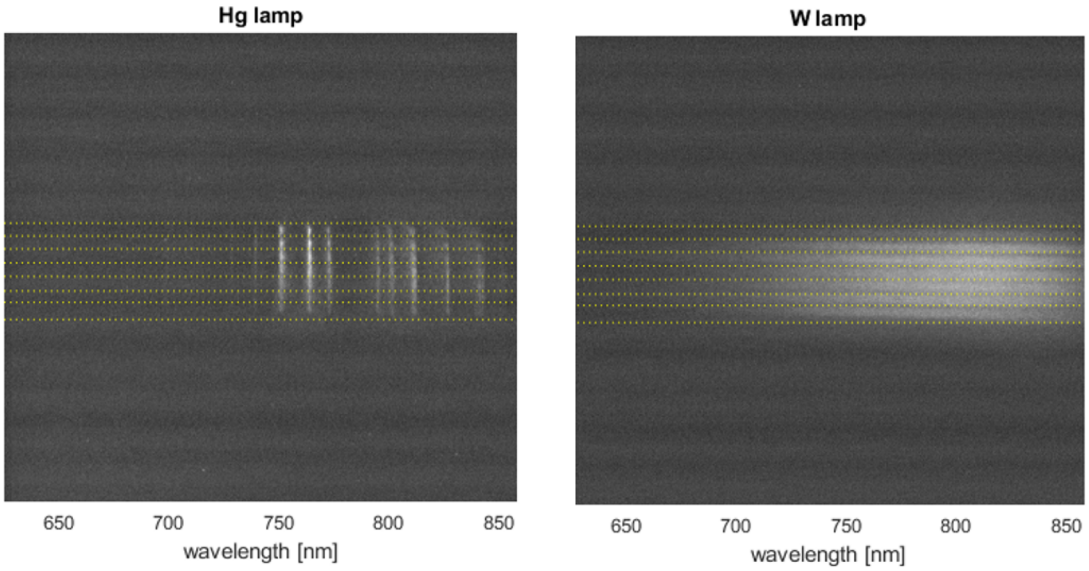

- Left: HG lamp line emission used to calibrate wavelength.
- Right: W lamp continuum emission used to calibrate amplitude.

Figure 12. Calibration spectra observed with DigiKrom-240 monochromator. Horizontal yellow dotted lines indicate the bounds of the seven fibers in the fiber bundle. The same calibration procedure applies to the new Isoplane 320.

with the 1200 groove/mm grating, 50 nm spectral range with the 600 groove/mm grating). Without astigmatism correction, the monochromator does not act as an imaging spectrometer, and some amount of aberration shifts the spectral and spatial distributions of the light output, which could confound measurements [27]. Furthermore, the monochromator uses gold-coated mirrors specialized for the infrared (IR) spectrum, which do not reflect light below 600 nm. Nonetheless, the platform still proved useful for determining how calibration procedures and for making initial surveys of the spectrum. Both the DigiKrom-240 and the Isoplane have gratings that can be rotated to adjust the center wavelength of the measured spectrum. A Hg gas lamp, which emits discrete atomic lines, is used to calibrate wavelengths at each center wavelength spectrum. A W filament lamp, which emits continuum radiation characteristic of a 3000 K black-body radiator, is used to calibrate amplitudes at each center wavelength setting. Line identification and broadening measurements rely on wavelength calibration, while line intensity ratio measurements depend on accurate amplitude calibration.

Different types of emission occur at distinct times during the plasma lifetime, and LIP generated with different pulses can exhibit different spectral output. In LIP generated by a 500 fs laser, molecular line emission occurs in the first 0.1 ns, continuum radiation dominates from 1–10 ns, and atomic line emission becomes most prevalent after 10 ns [28]. In LIP generated by a 48 fs pulse, molecular lines are observed immediately after the laser pulse, which is followed by atomic line radiation about 50-80 ps later. That study noted only weak continuum radiation [29]. The ICCD coupled with the spectrometer in this study has a minimum gate duration of 1.4 ns, but its gain of 1000 typically requires a gate time on the order of 20 ns to obtain sufficient signal for LIP generated with the Nd:YAG laser alone. Having a narrower time gate and therefore better time resolution could allow focused study of precisely the spectral components of interest as well as better time resolution of the plasma properties. This study is continuing to evaluate other sensor options including new ICCD cameras, streak cameras, and photo-multiplier tubes (PMTs).

Figure 13 exhibits spectra observed with the DigiKrom-240 from multiple time delays of a LIP generated by the Nd:YAG laser at full power on Aluminum solid targets. In data shown here, the YAG was focused with a 12.5 cm focal length lens, and the ICCD gate was set to 50 ns for early delay times and extends to 500 ns later in time (using MCP gain = 600 and CCD gain = 0). The spectra show an initial continuum burst, which decays and allows atomic spectra to dominate after about 200 ns. Nearly every visible atomic line is prevalent in literature studying LIP generated in air.

Moving forward, further effort needs to go into considering the accuracy of using atomic line emission extant at times after 200 ns to deduce the properties of LIP with lifetimes on the order of a few ns. Much of this work relates closely to the field of LIBS, and literature in that vein will inform further development of spectroscopic capabilities at NIWC Pacific.

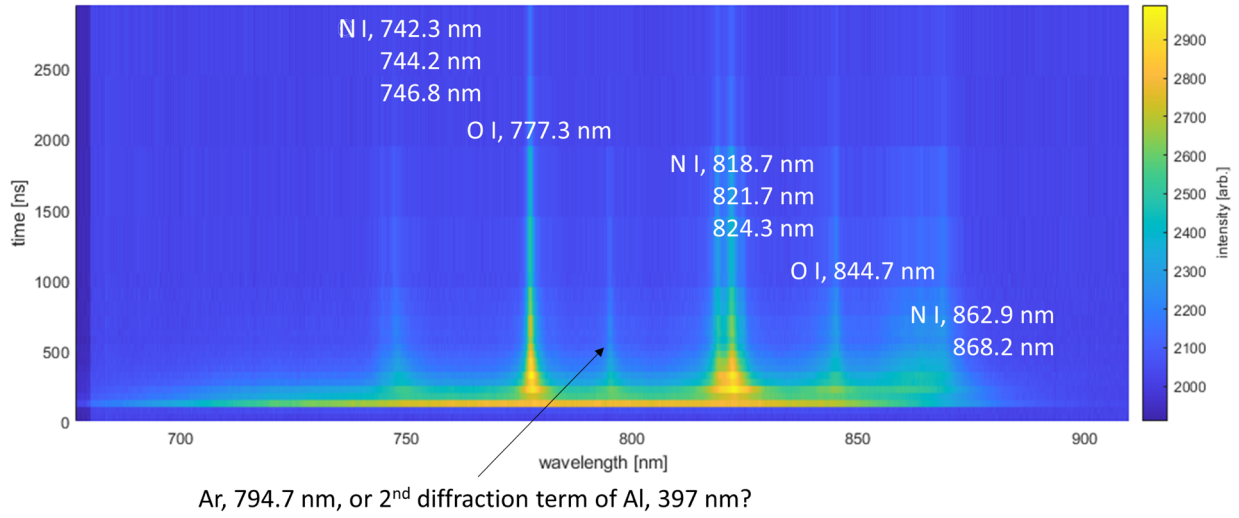

Figure 13. Contour plot of light emission showing the time evolution of spectral line emission from laser induced plasma generated by ns-duration Nd:YAG laser pulse on Aluminum metal target.

3.5 RF ANTENNA

Measurements of the RF output of the LIP are collected with a double ridge guide horn antenna (SAS-571) sensitive from 0.7-18 GHz digitized by a 16 GHz bandwidth Tektronix DPO71604C oscilloscope. The horn antenna is mounted to a grounded optics table and directed at the LIP region roughly 30 cm away. The antenna and oscilloscope are connected directly with a microwave cable with a cut-off frequency above 16 GHz, so the frequency response of the data acquisition system is limited by the oscilloscope. The scope is synchronized to trigger with a photodiode detector on the test bed optics table.

Without mitigation, noise from the Nd:YAG Q-switch has been picked up by the RF antenna even when the antenna is positioned over 3 m away from the laser head and is directed with its main lobe pointing away. Adding RF-absorbing foam to cover the optics table surfaces in the vicinity of the antenna and plasma formation region effectively eliminates the noise. To date, RF emission has been observed from LIP generated by the USPL incident on metal targets, but emission from LIP generated by the Nd:YAG has not been seen. Enhancement from overlapping the USPL and Nd:YAG lasers has also not been seen, but attempts to date have not sufficiently improved the repeatability of the location of Nd:YAG-generated plasma to ensure a proper test. Future efforts will focus on replicating RF enhancement by dual laser operation now that noise issues are mitigated and other diagnostics are in place.

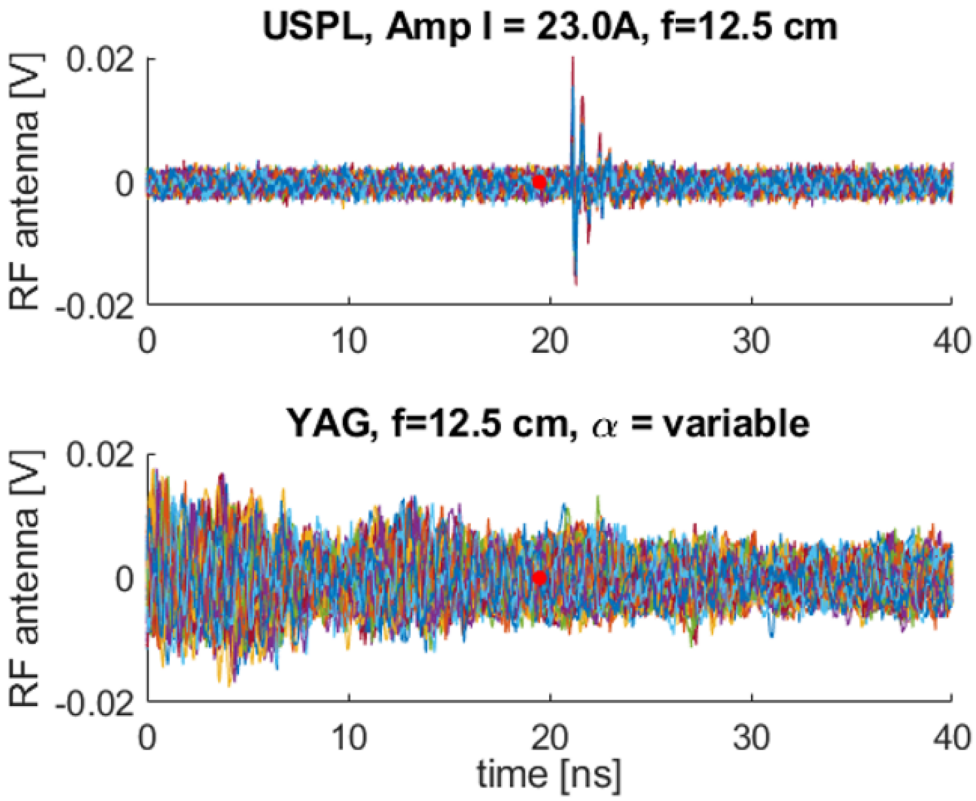

Top: RF emission detected by the horn antenna from a LIP generated by the USPL at maximum power focused with a 12.5 cm focal length lens.

Bottom: RF emission detected by the horn antenna from a LIP generated by the Nd:YAG at maximum power focused with a 12.5 cm focal length lens. Noise from the Nd:YAG Q-switch obscures any RF that may be emitted by the plasma. That noise has been mitigated by placing RF-absorbing foam flat on the optics table surfaces in the vicinity of the antenna and LIP formation region.

Figure 14. Measurements of RF emission acquired with horn antenna.

This page is intentionally blank.

4. CONCLUSION

A test bed to study RF emission by LIP has been constructed, and three diagnostics are being explored to study LIP. A USPL and a Nd:YAG laser have been synchronized to allow the replication of work that exhibited enhanced RF emission from the interplay of fs and ns-scale pulsed lasers in LIP generation. Significant effort has gone into understanding and building the spectroscopic and interferometric techniques necessary to spatially-resolve electron temperatures and electron densities. Initial RF emission measurements have been demonstrated with a directional RF antenna. Future work will focus on examining how RF enhancement relates to measured plasma properties, and it will examine RF enhancement by dual laser operation as a function of both time delay and relative laser intensity.

This page is intentionally blank.

REFERENCES

1. Varma, S., Spicer, J., Brawley, B., and Miragliotta, J. A. 2014. "Plasma enhancement of femtosecond laser-induced electromagnetic pulses at metal and dielectric surfaces," *Optical Engineering*, vol. 53, no. 5, p. 051515.

2. Henis, Z., Milikh, G., Papadopoulos, K., and Zigler, A. 2008. "Generation of controlled radiation sources in the atmosphere using a dual femtosecond/nanosecond laser pulse," *Journal of Applied Physics*, vol. 103, no. 10, p. 103111.

3. Tennant, A. and Fray, A. F. 1998. "A 64 element broad band volumetric array antenna," *IEEE Antennas and Propagation Society International Symposium. 1998 Digest. Antennas: Gateways to the Global Network. Held in conjunction with: USNC/URSI National Radio Science Meeting (Cat. No. 98CH36*, vol. 3 (pp. 1417–1420). IEEE.

4. Costa, B. F. and Abrão, T. 2018. "Closed-form directivity expression for arbitrary volumetric antenna arrays," *IEEE Transactions on Antennas and Propagation*, vol. 66, no. 12, pp. 7443–7448.

5. Buchanan, K., Jensen, J., Flores-Molina, C., Wheeland, S., and Huff, G. H. 2020. "Null Beamsteering using Distributed Arrays and Shared Aperture Distributions," *IEEE Transactions on Antennas and Propagation*.

6. Bolaños, J. G., Delikaris-Manias, S., Pulkki, V., Eskelinen, J., and Hæggström, E. 2014. "Laser-induced acoustic point source for accurate impulse response measurements within the audible bandwidth," *The Journal of the Acoustical Society of America*, vol. 135, no. 6, pp. EL298–EL303.

7. Eskelinen, J., Hæggström, E., Delikaris-Manias, S., Bolaños, J. G., and Pulkki, V. 2015. "Beamforming with a volumetric array of massless laser spark sources—Application in reflection tracking," *The Journal of the Acoustical Society of America*, vol. 137, no. 6, pp. EL389–EL395.

8. Labutin, T. A., Lednev, V. N., Ilyin, A. A., and Popov, A. M. 2016. "Femtosecond laser-induced breakdown spectroscopy," *Journal of Analytical Atomic Spectrometry*, vol. 31, no. 1, pp. 90–118.

9. Rusak, D. A., Castle, B. C., Smith, B. W., and Winefordner, J. D. 1997. "Fundamentals and applications of laser-induced breakdown spectroscopy," *Critical Reviews in Analytical Chemistry*, vol. 27, no. 4, pp. 257–290.

10. Nakajima, H., Shimada, Y., Somekawa, T., Fujita, M., and Tanaka, K. A. 2009. "Nondestructive sensor using microwaves from laser plasma by subnanosecond laser pulses," *IEEE Geoscience and Remote Sensing Letters*, vol. 6, no. 4, pp. 718–722.

11. Workman, J., Maksimchuk, A., Liu, X., Ellenberger, U., Coe, J. S., Chien, C.-Y., and Umstadter, D. 1996. "Picosecond soft-x-ray source from subpicosecond laser-produced plasmas," *JOSA B*, vol. 13, no. 1, pp. 125–131.

12. Kitaeva, G. K. 2008. "Terahertz generation by means of optical lasers," *Laser Physics Letters*, vol. 5, no. 8, pp. 559–576.

13. Tulej, M., Ligterink, N. F., de Koning, C., Grimaudo, V., Lukmanov, R., Keresztes Schmidt, P., Riedo, A., and Wurz, P. 2021. "Current Progress in Femtosecond Laser Ablation/Ionisation Time-of-Flight Mass Spectrometry," *Applied Sciences*, vol. 11, no. 6, p. 2562.

14. Li, X. and Guan, Y. 2020. “Theoretical fundamentals of short pulse laser–metal interaction: A review,” *Nanotechnology and Precision Engineering*, vol. 3, no. 3, pp. 105–125.

15. Couairon, A. and Mysyrowicz, A. 2007. “Femtosecond filamentation in transparent media,” *Physics Reports*, vol. 441, no. 2-4, pp. 47–189.

16. Aleksandrov, N. L., Bodrov, S. B., Tsarev, M. V., Murzanev, A. A., Sergeev, Y. A., Malkov, Y. A., and Stepanov, A. N. 2016. “Decay of femtosecond laser-induced plasma filaments in air, nitrogen, and argon for atmospheric and subatmospheric pressures,” *Physical Review E*, vol. 94, no. 1, pp. 1–7.

17. Peters, C. J., Shneider, M. N., and Miles, R. B. 2019. “Kinetics model of femtosecond laser ionization in nitrogen and comparison to experiment,” *Journal of Applied Physics*, vol. 125, no. 24, p. 243301.

18. Mortazavi, S., Parvin, P., Pour, M. M., Reyhani, A., Moosakhani, A., and Moradkhani, S. 2014. “Time-resolved evolution of metal plasma induced by Q-switched Nd: YAG and ArF-excimer lasers,” *Optics & Laser Technology*, vol. 62, pp. 32–39.

19. Varma, S. and Spicer, J. and Brawley, B. and Miragliotta, J. A. 2014. “Plasma enhancement of femtosecond laser-induced electromagnetic pulses at metal and dielectric surfaces,” *Optical Engineering*, vol. 53, no. 5, p. 051515.

20. Ross, M., Pascoguin, B., Hening, A., and Lynn, B. 2020. “Control of relative electron densities and spacing of two laser induced plasmas by spatial light modulation of femtosecond laser,” *Journal of Applied Physics*, vol. 128, no. 15, p. 154903.

21. Centurion, M., Pu, Y., and Psaltis, D. 2006. “Holographic capture of femtosecond pulse propagation,” *Journal of applied physics*, vol. 100, no. 6, p. 063104.

22. Rodriguez, G., Valenzuela, A. R., Yellampalle, B., Schmitt, M. J., and Kim, K. Y. 2008. “In-line holographic imaging and electron density extraction of ultrafast ionized air filaments,” *JOSA B*, vol. 25, no. 12, pp. 1988–1997.

23. Bernhardt, J., Liu, W., Théberge, F., Xu, H., Daigle, J., Châteauneuf, M., Dubois, J., and Chin, S. 2008. “Spectroscopic analysis of femtosecond laser plasma filament in air,” *Optics communications*, vol. 281, no. 5, pp. 1268–1274.

24. Pento, A. V., Bukharina, A. B., Nikiforov, S. M., Simanovsky, Y. O., Sartakov, B. G., Ablizen, R. S., Fabelinsky, V. I., Smirnov, V. V., and Grechnikov, A. A. 2021. “Laser-induced plasma on a metal surface for ionization of organic compounds at atmospheric pressure,” *International Journal of Mass Spectrometry*, vol. 461, p. 116498.

25. Bernhardt, J., Liu, W., Théberge, F., Xu, H. L., Daigle, J. F., Châteauneuf, M., Dubois, J., and Chin, S. L. 2008. “Spectroscopic analysis of femtosecond laser plasma filament in air,” *Optics Communications*, vol. 281, no. 5, pp. 1268–1274.

26. Vogman, G. and Shumlak, U. 2011. “Deconvolution of Stark broadened spectra for multi-point density measurements in a flow Z-pinch,” *Review of scientific instruments*, vol. 82, no. 10, p. 103504.

27. Yuan, Q., Zhu, D., Chen, Y., Guo, Z., Zuo, C., and Gao, Z. 2017. “Comparative assessment of astigmatism-corrected Czerny-Turner imaging spectrometer using off-the-shelf optics,” *Optics Communications*, vol. 388, pp. 53–61.

28. Martin, F., Mawassi, R., Vidal, F., Gallimberti, I., Comtois, D., Pepin, H., Kieffer, J., and Mercure, H. 2002. “Spectroscopic study of ultrashort pulse laser-breakdown plasmas in air,” *Applied spectroscopy*, vol. 56, no. 11, pp. 1444–1452.

29. Ilyin, A. A., Golik, S. S., and Shmirko, K. A. 2015. “Absorption and emission characteristics of femtosecond laser plasma filaments in the air,” *Spectrochimica Acta - Part B Atomic Spectroscopy*, vol. 112, pp. 16–22, URL http://dx.doi.org/10.1016/j.sab.2015.08.002.

This page is intentionally blank.

INITIAL DISTRIBUTION

84310	Technical Library/Archives	(1)
55280	Dr. M. P. Ross	(1)
55360	Melvin Pascoguin	(1)
55360	B Lynn	(1)

Defense Technical Information Center
Fort Belvoir, VA 22060–6218 (1)

This page is intentionally blank.

REPORT DOCUMENTATION PAGE

Form Approved
OMB No. 0704-01-0188

PLEASE DO NOT RETURN YOUR FORM TO THE ABOVE ADDRESS.

1. REPORT DATE *(DD-MM-YYYY)*	2. REPORT TYPE	3. DATES COVERED *(From - To)*
March 2022	Final	

4. TITLE AND SUBTITLE

Diagnostic Development For Study Of In-air Laser Induced Plasma.

5a. CONTRACT NUMBER

5b. GRANT NUMBER

5c. PROGRAM ELEMENT NUMBER

6. AUTHORS

Michael P. Ross, Ph.D.
Melvin Pascoguin
NIWC Pacific

5d. PROJECT NUMBER

5e. TASK NUMBER

5f. WORK UNIT NUMBER

7. PERFORMING ORGANIZATION NAME(S) AND ADDRESS(ES)

NIWC Pacific
53560 Hull Street
San Diego, CA 92152–5001

8. PERFORMING ORGANIZATION REPORT NUMBER

TR 3268

9. SPONSORING/MONITORING AGENCY NAME(S) AND ADDRESS(ES)

Office of Naval Research
875 N. Randolph Street
Arlington, VA 22203-1995

10. SPONSOR/MONITOR'S ACRONYM(S)

ONR

11. SPONSOR/MONITOR'S REPORT NUMBER(S)

12. DISTRIBUTION/AVAILABILITY STATEMENT

DISTRIBUTION STATEMENT A: Approved for public release. Distribution is unlimited.

13. SUPPLEMENTARY NOTES

Note: This report was created by Dr. Michael P. Ross who has moved on in his career and is no longer working at NIWC Pacific. Alternate contact Melvin Pascoquin (bienvenidomelvin.l.pascoquin.civ@us.navy.mil, 619-553-6012). This is a work of the United States Government and therefore is not copyrighted. This work may be copied and disseminated without restriction.

14. ABSTRACT

This study aims to explore the feasibility of generating Radio Frequency (RF) signals with laser induced plasma (LIP) in air at atmospheric pressure. This report presents the development status of a suite of diagnostics meant to look for correlations between LIP properties and RF emission. The study aims to control the time dynamics and geometry of LIP to determine if those factors ultimately control RF output. Adjusting the time delay between an ultra-short-pulse-laser (USPL) (35 fs pulse duration and 6 mJ pulse energy) and a Nd:YAG laser (ns pulse duration and up to 700 mJ pulse energy) allows control over the time dynamics. A spatial light modulator (SLM) provides control of the plasma geometry.

15. SUBJECT TERMS

RF signals, laser induced plasma; LIP correlation with RF emmission

16. SECURITY CLASSIFICATION OF:			17. LIMITATION OF ABSTRACT	18. NUMBER OF PAGES	19a. NAME OF RESPONSIBLE PERSON
a. REPORT	b. ABSTRACT	c. THIS PAGE			Brittany Lynn
U	U	U	SAR	40	19B. TELEPHONE NUMBER *(Include area code)* 619-553-5090

This page is intentionally blank.

This page is intentionally blank.

Naval Information Warfare Center Pacific (NIWC Pacific)
San Diego, CA 92152-5001